A Novel and Simple Torque Ripple Minimization Method of Synchronous Reluctance Machine Based on Torque Function Method

Hailong Wu, Daniel Depernet, Vincent Lanfranchi, Khadija Ei Kadri Benkara, and M. A. H. Rasid

***Abstract*—Synchronous reluctance machine (SynRM) has been studied widely in order to reduce its high torque ripple and improve its low power factor. This article proposes a torque ripple reduction method for SynRM by defining a novel parameter-torque function. With the help of torque function, the optimal currents aiming to compensate torque harmonics are obtained. The advantage of the proposed method is that torque function can be obtained easily and torque ripple reduction can be achieved by a simple control method. For the purpose of verifying the proposed method, both simulations and experiments are performed. Finally, the influence of power supply and parameter uncertainty on the proposed method has also been discussed.**

***Index Terms*—Optimal current, synchronous reluctance machine (SynRM), torque function, torque ripple.**

I. Introduction

THE synchronous reluctance machine (SynRM) has been studied widely since the last decade because of its simple and robust structure and high speed operation [1]–[3]. It can be applied to various fields, such as traction drive [4]–[6], automotive accessories [7], household [8], pumps, and fans [9]. However, its salient rotor topology produces high torque ripple which restricts the application of SynRM.

In order to minimize the high torque ripple of SynRM, different methods have been put forward. The mostly applied approach is to optimize its structure such as flux barriers [10]–[15], rotor rib [16], [17], rotor skewing [11], [18], and adding permanent magnet [19], [20]. Optimizing SynRM structure could produce satisfying result, but the design process is usually time-consuming.

The second idea to reduce torque ripple of SynRM is based on adding the selected current harmonics to the original sinusoidal stator currents. Yammine [21] analyzed the average torque of a two phase SynRM and defined the optimal current with several stator inductance harmonics. Decreasing each torque harmonic requires several current harmonics. So if several dominant torque harmonics are considered, the process of defining the relationship between each torque harmonic and the corresponding current harmonics could be time-consuming and complex. Besides, it is very difficult to define the optimal currents for a multiphase SynRM by the method presented in [21]. Truong *et al.* [22] measured stator inductances and their low order harmonics to calculate the optimal currents by electromagnetic torque equation. But, the accurate measurement of high stator inductance harmonics is very difficult. It means the optimal currents obtained by the measured inductances may not result in the optimal torque ripple reduction.

In this article, a novel parameter, torque function, is proposed for the purpose of decreasing torque ripple of SynRM easily by control method. With the help of torque function, all torque harmonics could be reduced theoretically by the calculated optimal currents. Moreover, torque function can be obtained easily by the finite-element method (FEM).

In addition, both simulations and experiments are performed and presented to validate the torque function and the torque ripple reduction method. The principles of analyzing the results are also put forward. During the experiment, the sensibility of measurement of the torque harmonics depends on the inertia of the load, which makes it difficult to determine the amplitude of harmonics. Hence, when the SynRM is controlled without load, a method is proposed to obtain torque harmonics by measuring rotor position.

A SynRM designed for an e-Clutch is manufactured and studied in this article. First, the manufacturing constraints limit the choice of rotor topology for this application. Besides, the minimum torque produced by the maximum available current is the first consideration for the studied e-Clutch. Compared with massive rotor and flux barriers rotor, the salient pole rotor topology provides better result [23]. Hence, the salient pole rotor is selected.

Manuscript received March 1, 2019; revised June 26, 2019 and October 17, 2019; accepted December 9, 2019. Date of publication January 3, 2020; date of current version October 19, 2020. *(Corresponding author: Hailong Wu.)*

H. Wu and D. Depernet are with the Bourgogne Franche-Comté, Femto-ST, 90000 Belfort, France (e-mail: hailong.wu@utbm.fr; daniel.depernet@utbm.fr).

V. Lanfranchi and K. E. K. Benkara are with the Sorbonne University, Université de Technologié de Compiegne, 60200 Compiègne, France (e-mail: vincent.lanfranchi@utc.fr; khadija.el-kadri-benkara@utc.fr).

M. A. H. Rasid is with the Faculty of Mechanical Engineering, Universiti Malaysia Pahang, Pekan 26600, Malaysia (e-mail: mahizami@ump.edu.my).

Color versions of one or more of the figures in this article are available online at http://ieeexplore.ieee.org.

Digital Object Identifier 10.1109/TIE.2019.2962490

II. Definition and Calculation of Torque Function

A. Electromagnetic Torque Equation

The electromagnetic torque of SynRM could be calculated by the co-energy $W(I,\theta_m)$

$$T_e = \frac{\partial W(I,\theta_m)}{\partial \theta_m} = \frac{P}{2}\sum_{i=1}^{3}\sum_{j=1}^{3} I_i I_j \frac{\partial L_{ij}(\theta)}{\partial \theta} \tag{1}$$

where θ_m is the mechanical rotor position and θ is the electrical position; P is the number of pole pairs; I is the stator current; i and j are the phase number of stator windings; L_{ij} is the stator self-inductance or mutual inductance.

The stator currents which can be represented by the currents of dq-axis and the stator inductances $L_{ij}(\theta)$ are introduced in the Appendix. Substituting the stator currents and stator inductances into (1), the torque (A3) containing all torque harmonics can be obtained as presented in the Appendix. More details about the derivation can be found in [24].

Furthermore, the SynRM can be controlled for different objectives by defining different current angles β. It is the angle between the current vector and d-axis current. For example, when current angle β is 45°, the maximum torque per ampere (MTPA) strategy is achieved in linear condition. As a result, a parameter k_{dq} can be defined to represent different current angles

$$k_{dq} = \frac{I_q}{I_d} = \tan\beta. \tag{2}$$

Substituting (2) into the torque (A3) in the appendix and separating the current and the inductance harmonics, the torque function $K_t(\theta,\beta,I)$ can be defined and calculated. It is introduced by (A4) in the Appendix.

Because the stator inductances contain many harmonics which are functions of rotor position and torque function contains stator inductances, torque function becomes also a function of rotor position. Besides, the function of current angle (2) is included in (A4), thus torque function is also a function of current angle to achieve different control objectives. When the magnetic saturation phenomenon appears in the SynRM, the stator inductances could be influenced. The saturation is linked to the stator current. Therefore, the stator inductances and torque function are also functions of stator current.

Based on torque function, the electromagnetic torque of SynRM can be represented

$$T_e = K_t(\theta,\beta,I)\, I_{ds23}^2 \tag{3}$$

where I_{ds23} is the current of d-axis obtained by the invariant Park transformation according to the stator currents.

B. Torque Ripple Reduction Method

The equation of torque function needs all stator inductance harmonics. It is obvious that based on stator inductances, the calculation of torque function is not convenient. According to (3), torque function can be calculated easily

$$K_t(\theta,\beta,I) = \frac{T_e}{I_{ds23}^2}. \tag{4}$$

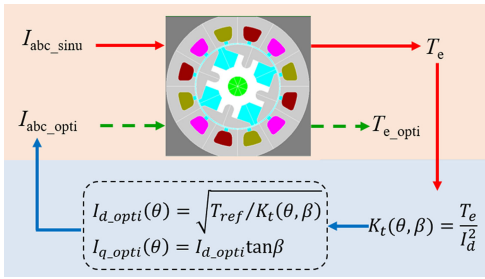

Fig. 1. Torque ripple reduction based on torque function.

For example, if the sinusoidal stator current is supplied to the finite element model of the SynRM, the electromagnetic torque can be obtained. The corresponding current of d-axis can be calculated. Consequently, the torque function could be calculated conveniently by (4).

The torque ripple reduction method is illustrated by Fig. 1 [25]. It is introduced for a salient pole SynRM in Fig. 1, but this method is also applicable for other rotor topologies of SynRM. In this article, saturation is not considered. So torque function $K_t(\theta,\beta,I)$ becomes $K_t(\theta,\beta)$. At first, the sinusoidal stator currents are supplied into the machine in order to calculate torque function. Then, the optimal currents in dq-axis can be calculated by the constant reference torque and torque function. In addition, the optimal stator currents can be obtained by the inverse Park transformation. Finally, the torque ripple could be minimized by supplying the optimal stator currents into SynRM.

The torque ripple minimization approach without saturation and with saturation has been analyzed and verified by FEM in [24]. When there is no saturation, the original currents and the corresponding optimal currents are introduced in Fig. 2. It can be observed that the stator currents without compensation are sinusoidal while the optimal stator currents contain many harmonics. The current of d-axis without compensation is constant while the optimal currents of dq-axis are not constant. The uncompensated torque and compensated torque are presented in Fig. 3. It can be observed that the torque ripple of the studied SynRM is minimized greatly.

III. Simulation

Torque control simulation, as presented in Fig. 4, is first performed in Simulink in order to test the proposed torque ripple reduction method. All stator inductance harmonics are obtained by finite element method in order to build the model of SynRM which can depict its torque ripple.

The reference peak value of stator current is calculated by the reference torque. When torque ripple is not compensated, it is calculated by the mostly used average torque equation

$$I_m^* = \sqrt{\frac{4T_{\text{ref}}}{3P(L_d - L_q)\sin 2\beta}} \tag{5}$$

where L_d and L_q are the average values of dq-inductances respectively and they are given in Table I.

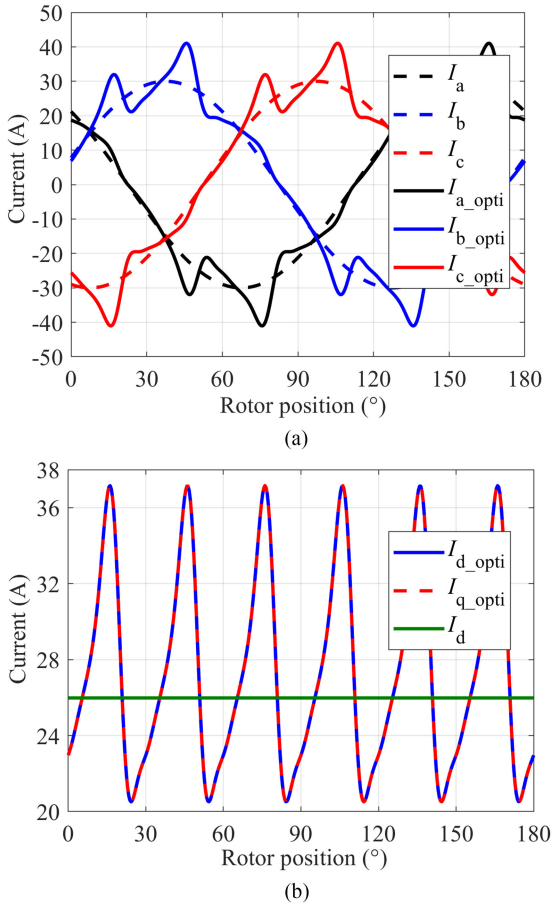

Fig. 2. Original currents and optimal currents ($\beta = 45°$, $I_m = 30$ A) of FEM. (a) Stator currents. (b) Currents of *dq*-axis.

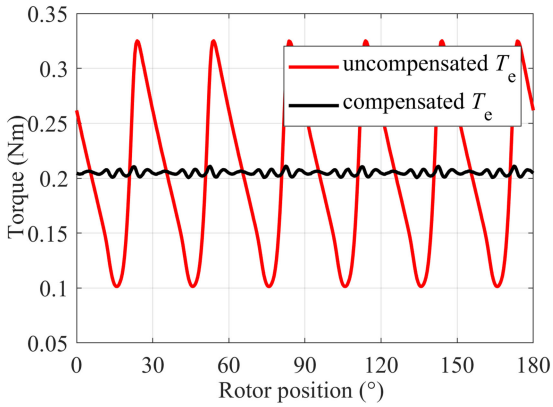

Fig. 3. Uncompensated torque and compensated torque of FEM ($\beta = 45°$).

The reference current with compensation is calculated based on torque function which is obtained by offline method

$$I_m^* = \sqrt{\frac{2T_{\text{ref}}}{3K_t(\theta,\beta)\cos^2\beta}}. \tag{6}$$

According to the reference current I_m^* and the power invariant Park transformation, the reference currents of *dq*-axis are

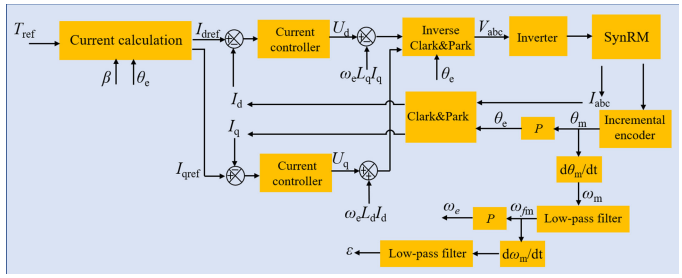

Fig. 4. Control diagram of torque ripple reduction based on torque function.

TABLE I
PARAMETERS OF THE STUDIED SYNRM

Parameter	Symbol	Quantity
d-axis inductance	L_d	2.55×10^{-4}H
q-axis inductance	L_q	1.1×10^{-4}H
Stator resistor	R	0.22 Ω
Gain of *d*-axis controller	K_d	0.46
Gain of *q*-axis controller	K_q	0.26
Maximal current	I_m	50A
Maximal voltage	U_m	12V/14V (assisted mode)
Dry friction torque	T_f	0.0011Nm
Viscous friction coefficient	f_ω	3.85×10^{-5} Nms
Inertia coefficient	J	1.43×10^{-3} kg·m^2
Number of pole pairs	P	2

obtained by the current angle β

$$\begin{cases} I_{d\text{ref}} = \sqrt{\frac{3}{2}} I_m^* \cos\beta \\ I_{q\text{ref}} = \sqrt{\frac{3}{2}} I_m^* \sin\beta \end{cases}. \tag{7}$$

The reference current calculation in Fig. 4 is represented by (5)–(7). It can be applied to any value of β. In this article, the MTPA control strategy is applied during simulation and experiment. So the current angle β is 45° in (5)–(7)

The PI controllers are used to regulate the *dq*-currents and they are designed as

$$\begin{cases} G_d(s) = K_d \dfrac{1 + \frac{L_d}{R}s}{\frac{L_d}{R}s} \\ G_q(s) = K_q \dfrac{1 + \frac{L_q}{R}s}{\frac{L_q}{R}s} \end{cases} \tag{8}$$

where s is the Laplace operator; R is the stator phase resistor, and $K_{d/q}$ is the gain of controllers as given in Table I.

According to these parameters, the closed loop bandwidths of *d*-axis and *q*-axis are calculated and both are 2360 Hz.

Fig. 5 presents torque function obtained by finite-element method for different current angles. It can be noticed that K_t is different at different β. To reduce torque ripple for different control strategies (β), different K_t should be applied. In this paper, $K_t(\beta = 45°)$ is used.

Besides, saturation is neglected during the simulation. Its influence on the proposed torque ripple reduction method has been analyzed in [24]. The torque reference is defined as 0.15 N·m

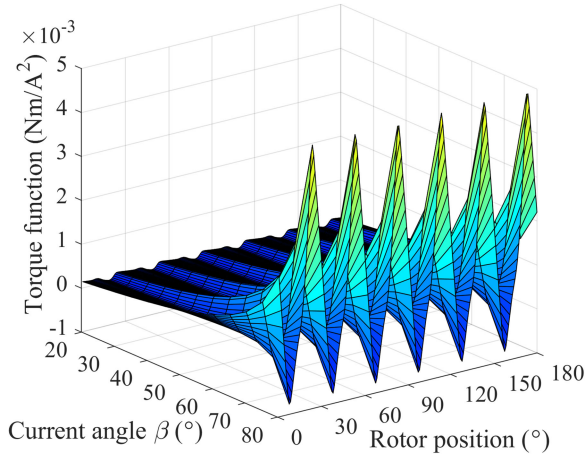

Fig. 5. Torque function for different β ($I_m = 30$A).

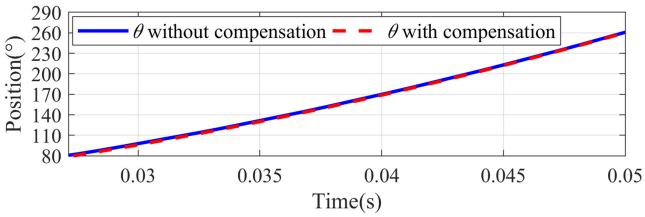

Fig. 6. Rotor position without compensation and with compensation.

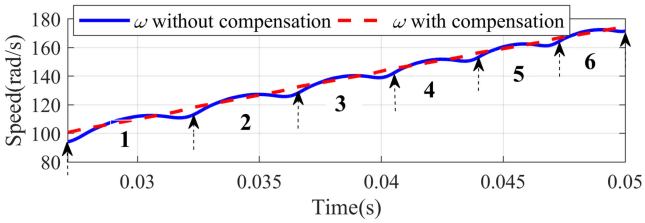

Fig. 7. Rotor speed without compensation and with compensation.

and the load torque is 0.1N·m. The inertia, the dry friction torque and the viscous friction coefficient are given in Table I.

The results in one electrical period of torque control simulation are introduced and studied. The rotor positions without compensation and with compensation are introduced in Fig. 6 and are applied to define one electrical period (180° mechanical rotor position). The corresponding rotor speeds are introduced by Fig. 7. It can be observed that the speed without compensation in one electrical period has six pulsations and the speed with compensation does not have noticeable pulsations.

Then, the accelerations of these two cases are calculated by the speeds and are presented in Fig. 8. In order to reduce the high noise in acceleration, an acceleration filter with the cutoff frequency 800 Hz is used. The design of this filter is based on the principles presented in Section IV-C.

It can be seen that the acceleration without torque ripple reduction has also six pulsations as illustrated in Fig. 8. Compared with the acceleration without compensation, the acceleration

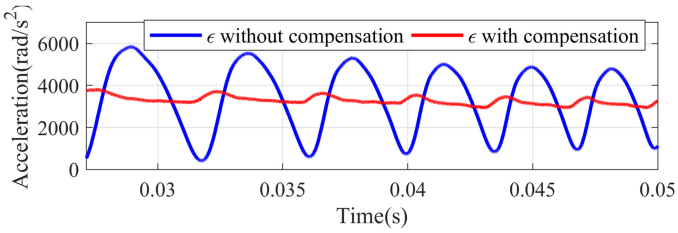

Fig. 8. Acceleration obtained by speed without compensation and with compensation.

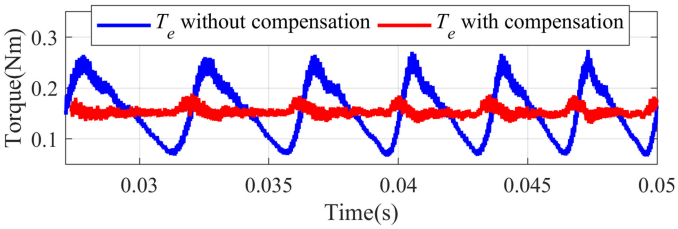

Fig. 9. Torque without compensation and with compensation.

with compensation is minimized greatly. The amplitudes of these two acceleration pulsations, especially the acceleration without compensation are reduced when the simulation time is longer. Because torque control is applied in the simulation. When the speed is larger, the viscous friction becomes larger. So the acceleration will become smaller until to zero when the total friction torque and load torque equal the reference torque.

In the simulation, the electromagnetic torque could be obtained easily. The torques without compensation and with compensation are presented in Fig. 9. It can be observed that the compensated torque is nearly constant while the uncompensated torque has high torque ripple. The harmonics of these two torques are introduced by Fig. 10. Comparing with the torque harmonics without compensation in Fig. 10(a), the dominant torque harmonics (6th and 12th) in Fig. 10(b) are minimized by supplying the optimal currents. As a conclusion, based on torque function, the proposed torque ripple reduction method could decrease torque harmonics effectively.

IV. Experiment

A. Experimental Setup

Experiment is preferred to verify the torque function-based torque ripple reduction method. But, mechanical disturbances of the connection of torque meter and of hysteresis break with the studied SynRM in the experimental bench make it difficult to measure electromagnetic torque harmonic accurately. Besides, the electromagnetic torque produced by the studied machine is small. It means the measured electromagnetic torque could be affected by the disturbing torque. Therefore, the electromagnetic torque could not be measured accurately by torque meter. The SynRM can be only controlled without load to not disturb the electromagnetic torque harmonic.

The control diagram is introduced in Fig. 4. The torque control without load is applied. The torque function ($\beta = 45°$) presented

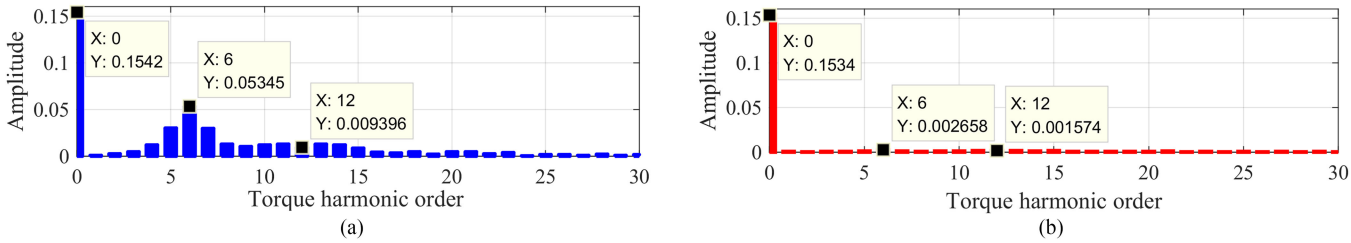

Fig. 10. Torque harmonics. (a) Without compensation. (b) With compensation.

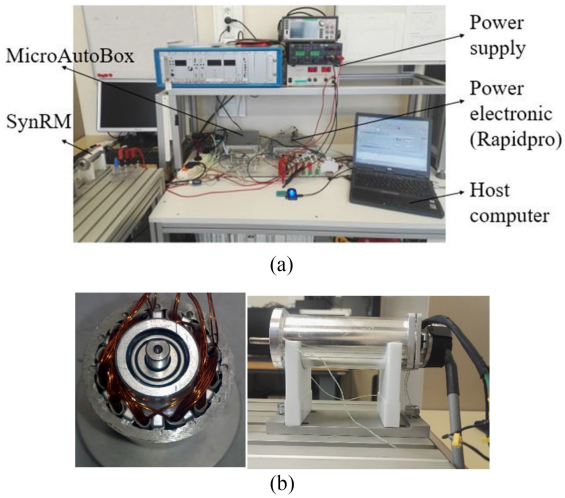

Fig. 11. Experimental platform. (a) dSPACE test bench. (b) Studied SynRM.

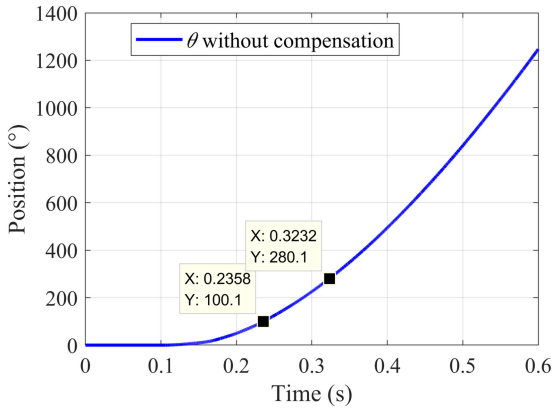

Fig. 12. Selected position data in one electrical period.

in Fig. 5 is used to calculate the reference current and compensate torque ripple during the experiment. Fig. 11(a) illustrates the experimental bench. It includes several parts: host computer, dSPACE MicroAutoBox and power electronic (Rapidpro) system, power supply and the studied SynRM. The studied SynRM is presented in Fig. 11(b).

An incremental encoder is used to measure the rotor position. The rotor speed is calculated by the measured position and is filtered by a low pass filter. The acceleration is obtained according to the speed.

B. Validation Approach

In order to test the proposed torque ripple reduction method, the electromagnetic torque should be calculated by the measured data. The dynamic equation of SynRM without load is introduced

$$T_e - T_f - f_\omega \omega_m = J\frac{d\omega_m}{dt} \tag{9}$$

where ω_m is the speed calculated by position.

Therefore, the electromagnetic torque could be calculated

$$T_e = J\frac{d\omega_m}{dt} + f_\omega \omega_m + T_f. \tag{10}$$

In (10), the dry friction torque T_f, the inertia J and the viscous friction coefficient f_ω are constant and have been measured as given in Table I.

C. Analysis Principles

In order to analyze the results of experiment, several principles should be presented first because the measured position signal needs to be treated and processed before that the useful information can be extracted.

1) One Electrical Period: Because the validation method is based on the torque control, the speed will be increased gradually. In order to reduce the influence of variation of the speed, it is better to analyze the torque measurement in one electrical period which means a mechanical angle of 180° as shown in Fig. 12. This period is enough and convenient to determine the torque harmonics.

The applied incremental encoder has a resolution of 500 cycles per revolution. This resolution is multiplied by four by the quadrature encoder pulse module of the control system. The position is then measured with a resolution of 2000 cycles per revolution.

2) Selection of Speed Range: According to the measured position, the corresponding speed could be calculated. The unfiltered speed as introduced in Fig. 13 has many harmonics. It cannot be applied to control the SynRM. This is mainly due to the low resolution of encoder. Therefore, the speed should be filtered and the result is also presented in Fig. 13. The design of the digital filter is explained in the following section.

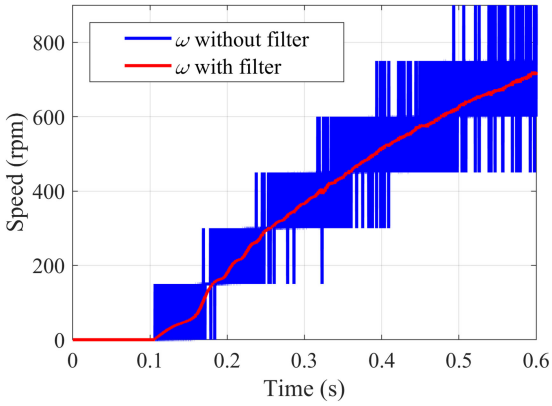

Fig. 13. Filtered and unfiltered speed in experiment.

Besides, during the experiment, the speed is increased gradually but the sampling frequency is constant. If the rotor speed is higher, it will contain fewer points than the lower speed during the same position length (180°). Then, the lower the speed during the measurement is, the greater the precision of the position measurement is. It is better to choose the rotor speed when it is low to analyze acceleration and torque.

3) Design of Speed Filter: The calculated speed contains many harmonics as presented in Fig. 13. In order to obtain useful information, it should be filtered by a low-pass filter. Besides, this filter could influence the speed harmonics and the calculated acceleration harmonics. Therefore, the frequency of the filter should be designed carefully.

The electrical frequency of the SynRM is

$$f_e = Pf_m = P\frac{\omega_m}{2\pi}. \tag{11}$$

The frequency of the m-th torque harmonic is

$$f_{me} = mf_e = mP\frac{\omega_m}{2\pi}. \tag{12}$$

If the mth torque harmonic is considered and compensated, the cut-off frequency of the speed filter should be higher than the frequency of the mth torque harmonic

$$f_c > f_{\mathrm{me}}. \tag{13}$$

The available order of torque harmonic is

$$m < \frac{f_c}{f_e} = \frac{2\pi f_c}{P\omega_m}. \tag{14}$$

Equation (14) presents the relationship among cut-off frequency, rotor speed and the order of torque harmonic. The available order of torque harmonic is proportional to the frequency f_c; but it is inversely proportional to the rotor speed. To analyze higher order torque harmonic, two methods are applicable. If the cut-off frequency of speed filter is fixed, the torque harmonics should be studied at low speed. If the selected speed range (in one electrical period) is fixed, the cut-off frequency of speed filter should be increased.

In the experiment, the cut-off frequency of the speed filter is fixed as f_c. The order of the dominant torque harmonic of the studied SynRM is m ($m = 6$, 12 in this article). The maximal speed can be calculated

$$\omega_m < \frac{2\pi f_c}{mP}. \tag{15}$$

In conclusion, the measured speed should be defined according to the electrical period, proper speed range and speed filter design.

D. Analysis of Results

Considering the speed limit and the limit of torque calculation, the torque reference is defined as 0.005 N·m. The rotor positions without compensation and with compensation are applied to present the electrical period and are shown in Fig. 14(a) and (b), respectively. The 6th and the 12th torque harmonics of the studied SynRM are dominant as introduced in Fig. 10(a). Thus, the maximum order of the dominant torque harmonic m is 12. The cut-off frequency of speed filter is defined as 250 Hz in experiment. Therefore, according to (15), the maximum speed during the analysis is

$$\omega_m < 65.45\,\mathrm{rad/s} = 625\ \mathrm{r/min}.$$

Then, the stator currents without compensation and with compensation are presented in Fig. 15(a) and (b) respectively. The rotor speeds without compensation and with compensation are introduced in Fig. 16(a) and (b), respectively. It can be noticed that the speed without compensation has six pulsations in one electrical period while the speed with compensation is smoother. In order to verify the proposed torque ripple reduction method, the accelerations of these two cases are calculated and presented in Fig. 17(a) and (b), respectively. The acceleration without compensation has also six obvious pulsations. Compared with the acceleration without compensation, the pulsations of the acceleration with compensation are reduced greatly.

According to (10), the electromagnetic torques without compensation and with compensation is calculated by the corresponding accelerations and are presented in Fig. 18. It can be seen that the uncompensated torque in Fig. 18(a) contains six pulsations. On the other side, the amplitudes of the compensated torque are decreased. The high-frequency torque harmonics in Fig. 18 are produced by the limitation of the low-pass filters.

In addition, the torque ripple reduction simulation in Flux 2-D is also performed in order to confirm the calculated electromagnetic torque by the experimental data. The produced torques in Flux 2-D without compensation and with compensation are also introduced in Fig. 18(a) and (b), respectively. It can be observed that the calculated torques of experiment is very close to those obtained by Flux 2-D except that the experimental torque contains more high frequency harmonics. Besides, the torque ripple is reduced from 109 to 4.9% which validates the proposed torque ripple reduction method.

Then, these two torques of experiment are analyzed and their harmonics are illustrated in Fig. 19. Compared with the torque harmonics in Fig. 19(a), it can be observed that the 6th and the 12th torque harmonics in Fig. 19(b) are decreased greatly by the proposed torque ripple reduction approach. According to the results of simulation and the experiment, it can be confirmed

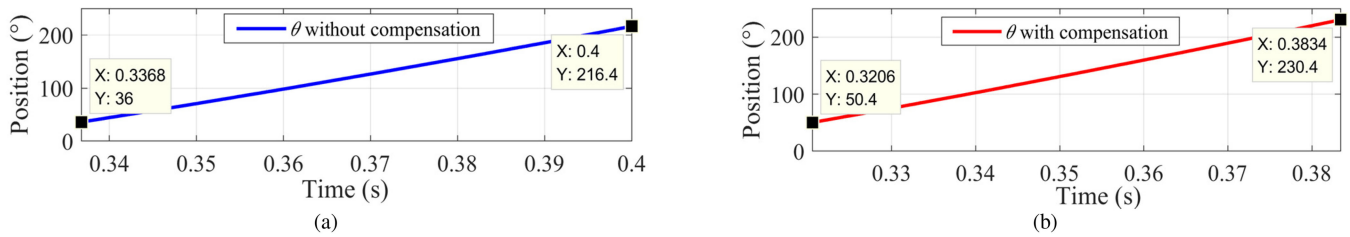

Fig. 14. Measured rotor position in experiment. (a) Without compensation. (b) With compensation.

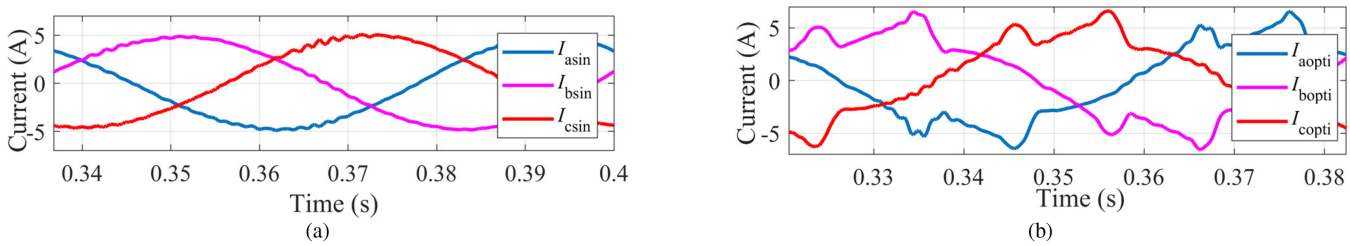

Fig. 15. Stator current in experiment. (a) Without compensation. (b) With compensation.

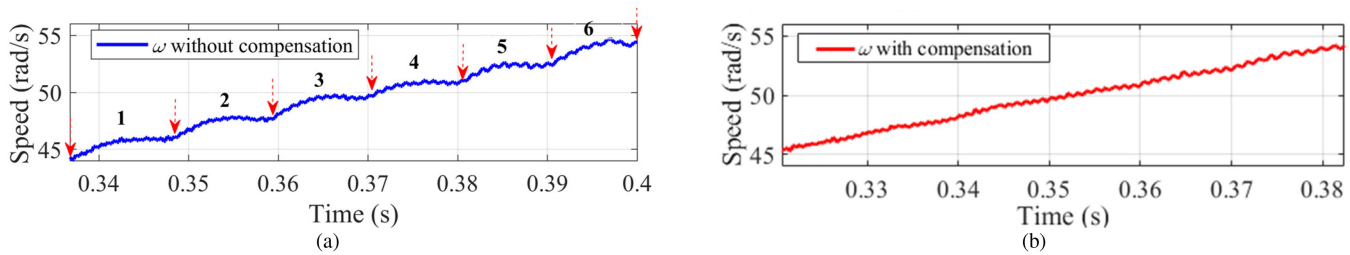

Fig. 16. Rotor speed calculated by position in experiment. (a) Without compensation. (b) With compensation.

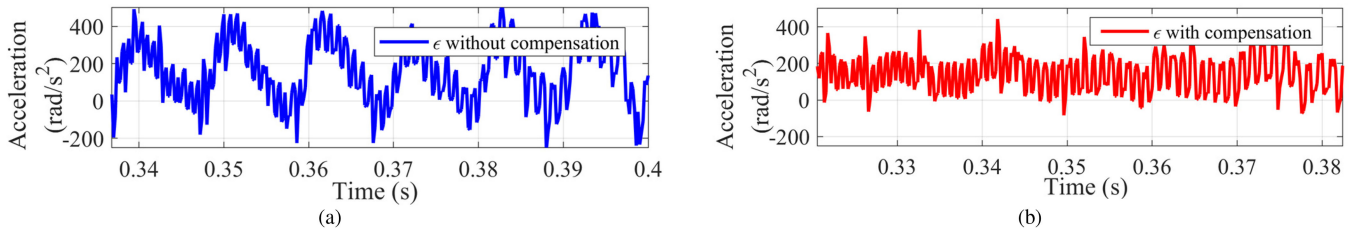

Fig. 17. Acceleration obtained by speed in experiment. (a) Without compensation. (b) With compensation.

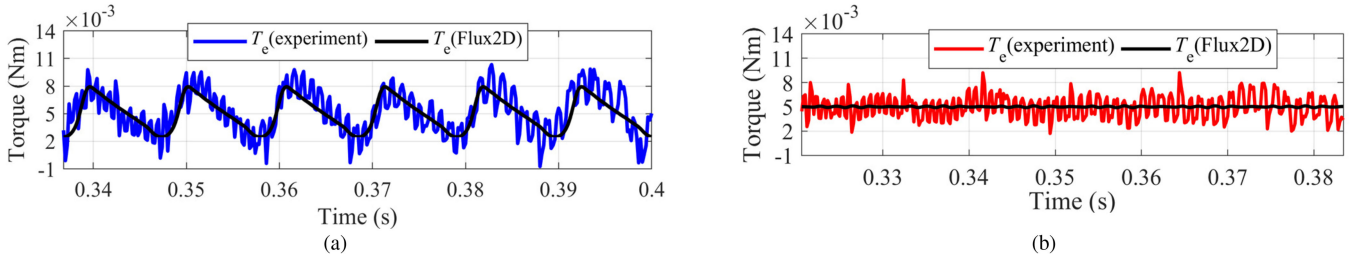

Fig. 18. Electromagnetic torque calculated in experiment. (a) Without compensation. (b) With compensation.

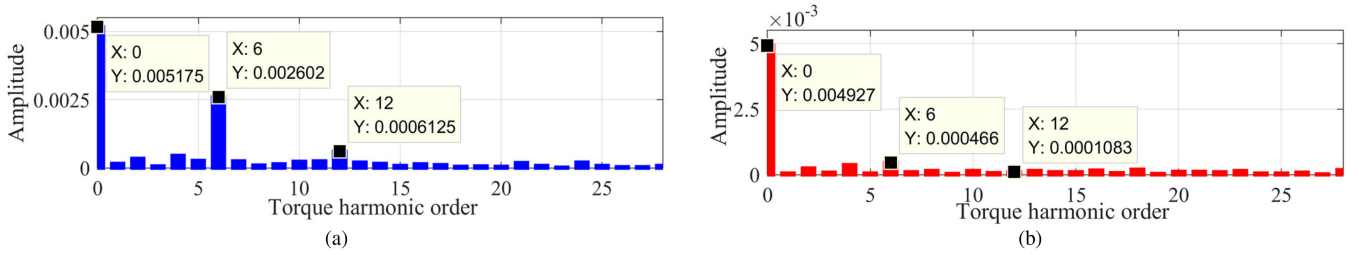

Fig. 19. Amplitudes of torque harmoics in experiment. (a) Without compensation. (b) With compensation.

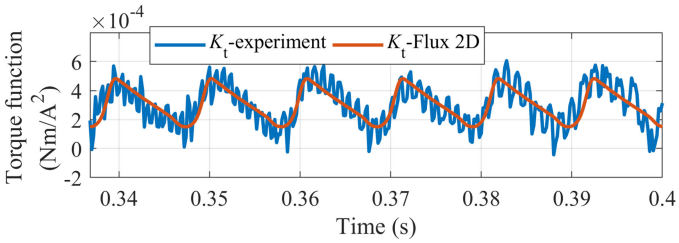

Fig. 20. Torque functions obtained by experiment and FEM.

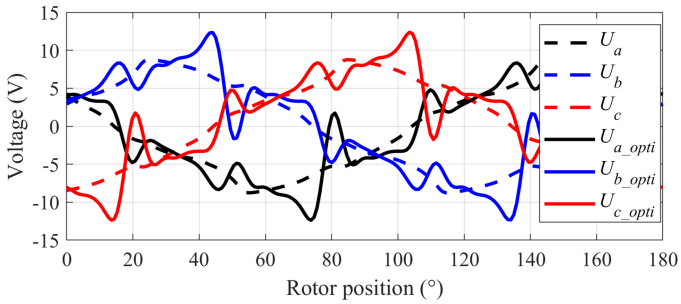

Fig. 21. Stator voltages without compensation and with compensation ($\beta = 45°$, $I_m = 30$ A, $\omega = 1500$ r/min).

that the torque ripple of the studied SynRM is minimized by the proposed torque ripple reduction method.

Finally, the torque function is also obtained during experiment and is presented in Fig. 20. According to (4), it is calculated by the uncompensated torque in Fig. 18(a) and the corresponding current I_d calculated by the stator currents in Fig. 15(a). Compared with the torque function obtained by finite-element simulation, it can be noticed that they are nearly identical except for the high harmonics of the measured torque function.

E. Discussion About the Proposed Method

1) Influence of Power Supply: The proposed torque ripple reduction method can compensate torque ripple effectively. On the other hand, it can be noticed in Figs. 2(a) and 15(b) the optimal currents are larger than the original sinusoidal stator currents. So, the stator voltages could also be changed when torque ripple is decreased which means the required power will be changed. It is better to analyze the influence of the increased power on the proposed method.

At first, the stator voltages corresponding to the simulation in Figs. 2 and 3 are presented by Fig. 21. The stator voltages without compensation in Fig. 21 are also not sinusoidal. Because the sinusoidal stator currents are defined as 30 A and the speed is kept as 1500 r/min. The high torque ripple leads to nonsinusoidal voltage. On the other side, the stator voltages with compensation are also nonsinusoidal. They are much larger than the voltages when torque ripple is not minimized. According to the corresponding optimal currents in Fig. 2(a), it is obvious that the required power should be increased to produce additional torque harmonics which are applied to compensate the original high torque harmonics.

When the sinusoidal stator current is kept as 30 A and current angle β is 45°, the produced average electromagnetic torque is 0.205 N·m. Then, the load torque is kept as 0.205 N·m and the maximum available speed without torque ripple reduction is 4300 r/min with the current limit and voltage limit as given in Table I. If the torque ripple is minimized for this load torque at higher speed (>1500 r/min), the increased power will limit the maximum available speed.

Then finite element simulation is performed to study the maximum available speed. The results show when the speed is 2200 r/min, the voltage reaches its maximum available value. Its means if speed is lower than 2200 r/min, torque ripple can be minimized. If speed is larger than 2200 r/min, the proposed method will be limited by the available voltage which means power supply. It should be stated that the limit of power supply on the proposed method depends on the reduced torque ripple. Its influence could not be so noniterable for other SynRM.

2) Influence of Measurement Errors on Torque Function: According to (4), two methods can be proposed to obtain torque function. The first one is based on FEM. This method is simple and efficient. But it requires the finite element model of machine which may be not available. The second approach is to measure K_t by experiment. This method can provide the actual torque function. But, the electromagnetic torque should be measured by torque meter accurately or be calculated by the dynamic equation as presented by (10). In Section IV, the torque function obtained by FEM is applied to confirm the proposed method and is also compared with the measured torque function. It illustrates that if there is no finite element model of a SynRM, torque function can also be measured accurately.

The dynamic equation method requires several mechanical parameters, such as inertia and viscous friction coefficient. If there exist errors in these mechanical parameters, the torque

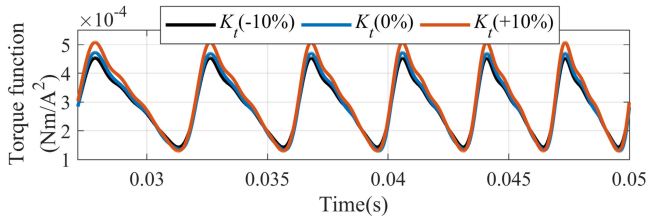

Fig. 22. Torque function with inertia error (10% and −10%).

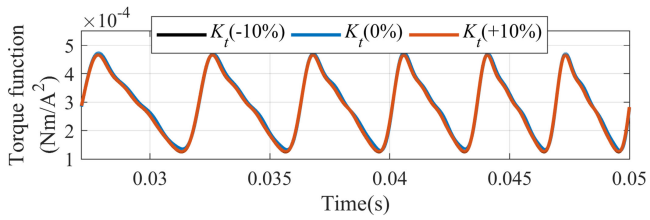

Fig. 23. Torque function with viscous coefficient error (10% and −10%).

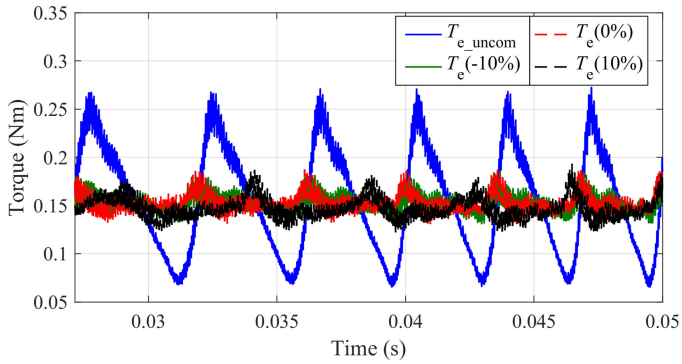

Fig. 24. Uncompensated torque and compensated torques by K_t with inertia error.

function could be influenced. Therefore, the influence of measurement errors of inertia and viscous friction coefficient (J and f_ω) on the proposed method are analyzed.

These two parameters have been given in Table I. It is assumed that there exist 10% and −10% errors from either J or f_ω. The simulation conditions (reference torque 0.15 N·m and load torque 0.1 N·m) are same as Section III. When torque ripple is not compensated, according to (4) the torque functions are calculated by the estimated torques with added errors of J and f_ω. They are presented by Figs. 22 and 23, respectively.

It can be seen that torque function with 10% inertia error $K_t(10\%)$ in Fig. 22 becomes larger at peaks and becomes smaller at valleys than torque function without error $K_t(0\%)$. On the contrary, torque function with −10% inertia error $K_t(-10\%)$ in Fig. 22 becomes smaller at peaks. Besides, torque function with viscous friction coefficient errors is hardly changed. Therefore, the inertia error has larger impact on torque function measurement for the studied machine. It will be further studied by compensating torque ripple.

Then, torque functions with inertia errors are applied to reduce torque ripple. The results are presented in Fig. 24. It

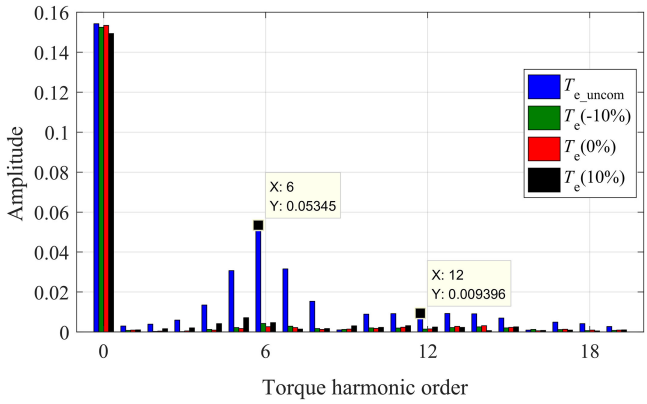

Fig. 25. Torque harmonics of compensated torques.

can be observed that compared with the uncompensated torque T_{e_uncom}, torque ripple is also reduced by applying $K_t(10\%)$ and $K_t(-10\%)$. Besides, the compensated torques $T_e(-10\%)$, $T_e(0\%)$ and $T_e(10\%)$ obtained by using $K_t(10\%)$, $K_t(-10\%)$ and $K_t(0\%)$, respectively are analyzed by fast Fourier transformation. The results are presented in Fig. 25. It indicates that the 6th and 12th torque harmonics are decreased greatly. Besides, the difference among these compensated torques is very small. As a result, inertia error could influence torque function, but can hardly affect the compensated results for the studied SynRM. The measurement of torque function is robust to mechanical parameter uncertainties.

V. Conclusion

A novel parameter, torque function was proposed in this article. Based on torque function, a torque ripple reduction method was put forward. This approach was simple to be applied. Several analyzing principles, such as speed range and design of speed filter were also introduced to implement an accurate measuring method of electromagnetic torque harmonic. The results of simulation and experiment showed that the torque ripple of the studied SynRM was decreased by more than 95%. On the other hand, the proposed method required more power to reduce torque ripple. The increased power requirement could limit the method. The analysis showed that the torque function method was robust to mechanical parameter uncertainties.

In the future, the proposed method will be applied for high power SynRM at high speed with different loads. Besides, the limit of PWM frequency on the proposed method should also be studied further.

Appendix

The stator currents can be calculated by the power invariant Park transformation

$$\begin{bmatrix} I_a \\ I_b \\ I_c \end{bmatrix} = \sqrt{\frac{2}{3}} \begin{bmatrix} \cos\theta & -\sin\theta \\ E\left(\theta - \frac{2\pi}{3}\right) & -\sin\left(\theta - \frac{2\pi}{3}\right) \\ \cos\left(\theta - \frac{4\pi}{3}\right) & -\sin\left(\theta - \frac{4\pi}{3}\right) \end{bmatrix} \begin{bmatrix} I_{ds23} \\ I_{qs23} \end{bmatrix}. \tag{A1}$$

$$\boldsymbol{L}_{ij}(\theta)=\begin{bmatrix}\sum_{k=0,2,4\ldots}L_k\cos(k\theta) & \sum_{k=0,2,4\ldots}M_k\cos\left(k\left(\theta+^{2\pi}/_{3}\right)\right) & \sum_{k=0,2,4\ldots}M_k\cos\left(k\left(\theta-^{2\pi}/_{3}\right)\right)\\ \sum_{k=0,2,4\ldots}M_k\cos\left(k\left(\theta+^{2\pi}/_{3}\right)\right) & \sum_{k=0,2,4\ldots}L_k\cos\left(k\left(\theta-^{2\pi}/_{3}\right)\right) & \sum_{k=0,2,4\ldots}M_k\cos(k\theta)\\ \sum_{k=0,2,4\ldots}M_k\cos\left(k\left(\theta-^{2\pi}/_{3}\right)\right) & \sum_{k=0,2,4\ldots}M_k\cos(k\theta) & \sum_{k=0,2,4\ldots}L_k\cos\left(k\left(\theta+^{2\pi}/_{3}\right)\right)\end{bmatrix} \tag{A2}$$

$$T_e=P\left(\frac{-k}{2}\right)\left\{\begin{array}{l}\left[\sum_{k=m_1}\frac{L_k+2M_k}{2}\sin(k-2)\theta+\sum_{k=m_2}\frac{L_k+2M_k}{2}\sin(k+2)\theta+\sum_{k=m_3}(L_k-M_k)\sin k\theta\right]I_{ds23}^2\\ +\left[-\sum_{k=m_1}\frac{L_k+2M_k}{2}\sin(k-2)\theta-\sum_{k=m_2}\frac{L_k+2M_k}{2}\sin(k+2)\theta+\sum_{k=m_3}(L_k-M_k)\sin k\theta\right]I_{qs23}^2\\ +\left[-\sum_{k=m_1}(L_k+2M_k)\cos(k-2)\theta+\sum_{k=m_2}\frac{L_k+2M_k}{2}\cos(k+2)\theta\right]I_{ds23}I_{qs23}\end{array}\right\} \tag{A3}$$

$$\begin{aligned}&K_t(\theta,\beta,I)\\&=P\left(\frac{-k}{2}\right)\left\{\begin{array}{l}\left[\sum_{k=m_1}\frac{L_k+2M_k}{2}\sin(k-2)\theta+\sum_{k=m_2}\frac{L_k+2M_k}{2}\sin(k+2)\theta+\sum_{k=m_3}(L_k-M_k)\sin k\theta\right]\\ +\left[-\sum_{k=m_1}\frac{L_k+2M_k}{2}\sin(k-2)\theta-\sum_{k=m_2}\frac{L_k+2M_k}{2}\sin(k+2)\theta+\sum_{k=m_3}(L_k-M_k)\sin k\theta\right]k_{dq}^2\\ +\left[-\sum_{k=m_1}(L_k+2M_k)\cos(k-2)\theta+\sum_{k=m_2}\frac{L_k+2M_k}{2}\cos(k+2)\theta\right]k_{dq}\end{array}\right\}\end{aligned} \tag{A4}$$

The stator inductances are defined as in (A2) shown at the top of the page, where L_k and M_k are the amplitudes of kth self-inductance and kth mutual-inductance.

The torque equation containing all torque harmonics is obtained in (A3) and (A4) shown at the top of the page, where the orders of torque harmonics are

$$\begin{cases}m_1=2,8,14,20,\ldots\\ m_2=4,10,16,22,\ldots\\ m_3=6,12,18,24,\ldots\end{cases}. \tag{A5}$$

REFERENCES

[1] X. Zhang and G. H. B. Foo, "Overmodulation of constant-switching-frequency-based DTC for reluctance synchronous motors incorporating field-weakening operation," *IEEE Trans. Ind. Electron.*, vol. 66, no. 1, pp. 37–47, Jan. 2019.

[2] S. Bolognani, L. Ortombina, F. Tinazzi, and M. Zigliotto, "Model sensitivity of fundamental-frequency-based position estimators for sensorless PM and reluctance synchronous motor drives," *IEEE Trans. Ind. Electron.*, vol. 65, no. 1, pp. 77–85, Jan. 2018.

[3] A. Arafat and S. Choi, "Optimal phase advance under fault-tolerant control of a five-phase permanent magnet assisted synchronous reluctance motor," *IEEE Trans. Ind. Electron.*, vol. 65, no. 4, pp. 2915–2924, Apr. 2018.

[4] N. Bianchi, S. Bolognani, E. Carraro, M. Castiello, and E. Fornasiero, "Electric vehicle traction based on synchronous reluctance motors," *IEEE Trans. Ind. Appl.*, vol. 52, no. 6, pp. 4762–4769, Nov./Dec. 2016.

[5] T. A. Huynh and M.-F. Hsieh, "Comparative study of PM-assisted SynRM and IPMSM on constant power speed range for EV applications," *IEEE Trans. Magn.*, vol. 53, no. 11, pp. 1–6, Nov. 2017, Art. no. 8211006.

[6] E. Trancho *et al.*, "PM-assisted synchronous reluctance machine flux weakening control for EV and HEV applications," *IEEE Trans. Ind. Electron.*, vol. 65, no. 4, pp. 2986–2995, Apr. 2018.

[7] M. A. H. Rasid *et al.*, "Preliminary thermal evaluation of actuator for Steer-by-Wire vehicle," *IEEE Trans. Veh. Technol.*, vol. 67, no. 12, pp. 11468–11474, Dec. 2018.

[8] O. Payza, Y. Demir, and M. Aydin, "Investigation of losses for a concentrated winding high-speed permanent magnet-assisted synchronous reluctance motor for washing machine application," *IEEE Trans. Magn.*, vol. 54, no. 11, pp. 1–5, Nov. 2018.

[9] M. Palmieri, M. Perta, and F. Cupertino, "Design of a 50.000-r/min synchronous reluctance machine for an aeronautic diesel engine compressor," *IEEE Trans. Ind. Appl.*, vol. 52, no. 5, pp. 3831–3838, Sep./Oct. 2016.

[10] H. A. Moghaddam, A. Vahedi, and S. H. Ebrahimi, "Design optimization of transversely laminated synchronous reluctance machine for flywheel energy storage system using response surface methodology," *IEEE Trans. Ind. Electron.*, vol. 64, no. 12, pp. 9748–9757, Dec. 2017.

[11] N. Bianchi, M. Degano, and E. Fornasiero, "Sensitivity analysis of torque ripple reduction of synchronous reluctance and interior PM motors," *IEEE Trans. Ind. Appl.*, vol. 51, no. 1, pp. 187–195, Jan./Feb. 2015.

[12] E. Howard, M. J. Kamper, and S. Gerber, "Asymmetric flux barrier and skew design optimization of reluctance synchronous machines," *IEEE Trans. Ind. Appl.*, vol. 51, no. 5, pp. 3751–3760, Sep./Oct. 2015.

[13] M. Barcaro, T. Pradella, and I. Furlan, "Low-torque ripple design of a ferrite-assisted synchronous reluctance motor," *IET Elect. Power Appl.*, vol. 10, pp. 319–329, 2016.

[14] S. Taghavi and P. Pillay, "A novel grain-oriented lamination rotor core assembly for a synchronous reluctance traction motor with a reduced torque ripple algorithm," *IEEE Trans. Ind. Appl.*, vol. 52, no. 5, pp. 3729–3738, Sep./Oct. 2016.

[15] D. Yan, C. Xia, L. Guo, H. Wang, and T. Shi, "Design and analysis for torque ripple reduction in synchronous reluctance machine," *IEEE Trans. Magn.*, vol. 54, no. 11, pp. 1–5, Nov. 2018.

[16] C. Babetto, G. Bacco, and N. Bianchi, "Design methodology for high-speed synchronous reluctance machines," *IET Elect. Power Appl.*, vol. 12, pp. 1110–1116, 2018.

[17] C. M. Donaghy-Spargo, "Electromagnetic–mechanical design of synchronous reluctance rotors with fine features," *IEEE Trans. Magn.*, vol. 53, no. 11, pp. 1–8, Nov. 2017, Art no. 8206308.

[18] S. R. Bonthu, M. T. B. Tarek, and S. Choi, "Optimal torque ripple reduction technique for outer rotor permanent magnet synchronous reluctance motors," *IEEE Trans. Energy Convers.*, vol. 33, no. 3, pp. 1184–1192, Sep. 2018.

[19] H.-C. Liu, I.-G. Kim, Y. J. Oh, J. Lee, and S.-C. Go, "Design of permanent magnet-assisted synchronous reluctance motor for maximized back-EMF and torque ripple reduction," *IEEE Trans. Magn.*, vol. 53, no. 6, pp. 1–4, Jun. 2017, Art no. 820260.

[20] T. A. Huynh, M.-F. Hsieh, K.-J. Shih, and H.-F. Kuo, "An investigation into the effect of PM arrangements on PMa-SynRM performance," *IEEE Trans. Ind. Appl.*, vol. 54, no. 6, pp. 5856–5868, Nov./Dec. 2018.

[21] S. Yammine, "Contribution to the synchronous reluctance machine performance improvement by design optimization and current harmonics injection," Ph.D. dissertation, LAPLACE, Univ. Toulouse, Toulouse, France, 2015.

[22] P. H. Truong, D. Flieller, N. K. Nguyen, J. Mercklé, and G. Sturtzer, "Torque ripple minimization in non-sinusoidal synchronous reluctance motors based on artificial neural networks," *Elect. Power Syst. Res.*, vol. 140, pp. 37–45, 2016.

[23] C. Doc, "Contribution à la conception et au dimensionnement d'un actionneur d'embrayage," Ph.D. dissertation, LEC, UTC, Compiègne, France, 2010.

[24] H. Wu, D. Depernet, and V. Lanfranchi, "Analysis of torque ripple reduction in a segmented-rotor synchronous reluctance machine by optimal currents," *Math. Comput. Simul.*, vol. 158, pp. 130–147, 2019.

[25] H. Wu, D. Depernet, and V. Lanfranchi, "Comparison of torque ripple reductions and copper losses of three synchronous reluctance machines," in *Proc. IEEE Veh. Power Propulsion Conf.*, 2017, pp. 1–6.

Hailong Wu received the Ph.D. degree in electrical engineering from Université Bourgogne Franche-Comté, Belfort, France, in 2019.

He is currently a Postdoc with the Laboratory of Electrical Engineering and Power Electronics. His main research interests include multiphysic optimization and control strategies of electrical machines.

Daniel Depernet received the Ph.D. degree in electrical engineering from the University of Reims Champagne-Ardenne, Reims, France, in 1995.

He is currently Associate Professor of electrical engineering with the University of Belfort-Montbéliard. His teaching areas include sensors, digital signal processing, and real time control. He is also a Researcher with the Department of Energy, Franche-Comtè Electronics Mechanics Thermal Science and Optics–Sciences and Technologies (FEMTO-ST) Institute. His main research interests are control of electrical drives and power sources diagnosis.

Vincent Lanfranchi received the Ph.D. degree in electrical engineering from the University of Reims, Reims, France, in 2000.

He is currently a Full Professor with the Université de Technologie de Compiègne, Compiègne, France. His teaching areas are electrical engineering and mechatronic. He is a Researcher with the ROBERVAL Laboratory of Mechanic and Electric Energy. His main research interests include design of electrical systems with multiphysic approach. It also focuses on harmonic behavior including converter-machine interactions, pulsewidth modulation strategies and machine control.

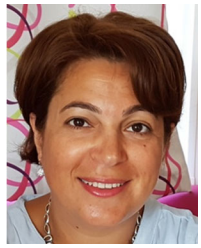

Khadija Ei Kadri Benkara received the Dipl.-Eng. degree in electrical engineering from the Ecole Nationale Supérieure d'Electrotechnique, d'Electronique, d'Informatique et d'Hydraulique de Toulouse, Toulouse, France, in 1998, and the Ph.D. degree in engineering sciences from the University of Technology of Belfort-Montbéliard, Belfort, France, and University of Besançon, Besançon, France, in 2006.

She is currently a Research Engineer with the University of Compiègne in Roberval Laboratory, Compiègne, France. Her research activities concern multiphysic modeling of electric actuators and energy sources and application to electric/hybrid vehicle.

M. A. H. Rasid received the Ph.D. degree in mechatronics from the Université de Technologie de Compiègne, Compiègne, France, in 2016.

He is currently a Senior Lecturer with the Faculty of Mechanical and Automotive Engineering Technology, Universiti Malaysia Pahang, Pahang, Malaysia. His teaching areas include electrical engineering, mechatronics and automatics. He is also a Researcher belonging to the Energy Sustainability Focus Group. His research interests include electromechanical systems with multiphysic approach, focusing on thermal, and vibroacoustic behavior.